An article presented by Professor Lilong Jiang *et al*. from Fuzhou University, China and Professor Hongyan He *et al*. from Institute of Process Engineering, CAS, China.

Insights into the electrochemical degradation of phenolic lignin model compounds in a protic ionic liquid–water system

The electrochemical degradation mechanism of phenolic lignin model compounds with typical C_{aryl}–O bonds in a protic IL-water system is clarified, including direct oxidation of substrates at the electrode and indirect oxidation by *in situ* generated H_2O_2.

As featured in:

See Lilong Jiang, Hongyan He *et al.*, *Green Chem.*, 2021, **23**, 1665.

ROYAL SOCIETY OF CHEMISTRY

rsc.li/greenchem

Registered charity number: 207890

Green Chemistry

PAPER

View Article Online
View Journal | View Issue

Cite this: *Green Chem.*, 2021, **23**, 1665

Insights into the electrochemical degradation of phenolic lignin model compounds in a protic ionic liquid–water system†

Guangyong Liu,‡[a,b] Qian Wang,‡[a] Dongxia Yan,[a] Yaqin Zhang,[a] Chenlu Wang,[a] Shijing Liang,[b] Lilong Jiang *[b] and Hongyan He *[a,c]

Cleavage of aryl ether (C_{aryl}–O) bonds is crucial for the conversion and value-added utilization of lignin and its derivatives, but remains extremely challenging under mild conditions due to strong C_{aryl}–O linkages. In this study, the C_{aryl}–O bond breaking is achieved through electrocatalytic oxidation of four phenolic lignin model compounds with typical C_{aryl}–O bonds, *i.e.*, 4-ethoxyphenol (EP), 4-phenoxyphenol (PP), *p*-benzyloxyphenol (PBP), and 2-(2-phenylethoxy)phenol (2-PEP), in a protic ionic liquid [BSO_3Hmim][OTf]–H_2O electrolyte, and the electrocatalytic oxidation mechanism is also fully explored. The effects of H_2O on the viscosity and conductivity of the [BSO_3Hmim][OTf] ionic liquid system, as well as the solubility and diffusion coefficients of O_2 and the four lignin substrates, are investigated to optimize the optimal ratio of the electrolyte system composed of [BSO_3Hmim][OTf] and H_2O. Electrochemical oxidation–reduction behaviors of the four lignin substrates in the [BSO_3Hmim][OTf]–H_2O system and the effect of O_2 and N_2 atmospheres on degradation are studied in detail by using cyclic voltammetry (CV) curves. Finally, by combining the analysis of degradation products with isotope labeling experiments, the C–O bond cleavage mechanism is obtained, which mainly involves direct and indirect oxidation. Specifically, under a N_2 atmosphere, the substrates are oxidized directly on the RuO_2-IrO_2/Ti mesh electrode through C_{aryl}–O bond splitting to form quinone and carbonium ions, while under an O_2 atmosphere, apart from the direct oxidation on the electrode, indirect oxidation of the lignin substrates also occurs through *in situ* generated H_2O_2. This study may provide some insight into developing effective strategies for efficient utilization of lignin under mild conditions.

Received 20th October 2020,
Accepted 22nd December 2020

DOI: 10.1039/d0gc03551c

rsc.li/greenchem

1. Introduction

Due to the limitation of fossil resources and their impact on the prominent greenhouse effect, researchers are making great efforts to develop sustainable and alternative feedstocks to supply fuels and chemicals.[1,2] Renewable biomass has attracted extensive attention from academia and industry due to its wide distribution, carbon-neutrality, less pollution, and low cost. Lignocellulosic biomass is the most abundant biological energy source on the planet, mainly consisting of cellulose (30–50%), hemicellulose (20–35%), and lignin (15–35%).[3–9] So far, cellulose and hemicellulose have been widely and well used in industry, whereas lignin is mostly considered as a kind of low-value residue. For instance, in the pulp and paper industry, only 2% of lignin is used commercially, although it is one of the most abundant and renewable natural biopolymers.[6,10] This situation arises from the fact that the diversity of three-dimensional complex amorphous polymer structures and rigid linkage units in lignin are affected by the type of plant and the specific process.[4] However, lignin is the only component that contains an aromatic structure in lignocellulose, which can be converted into various small molecular aromatic compounds with high added value through different depolymerization methods. As a kind of carbon-containing renewable energy source, the conversion and utilization of lignin have exhibited excellent potential in biochemistry, energy chemical industry, and other fields.

Lignin is primarily composed of three monolignol units, *i.e.*, sinapyl alcohol, coniferyl alcohol, and *p*-coumaryl alcohol.

[a]*CAS Key Laboratory of Green Process and Engineering, State Key Laboratory of Multiphase Complex Systems, Beijing Key Laboratory of Ionic Liquids Clean Process, Institute of Process Engineering, Chinese Academy of Sciences, Beijing 100190, China. E-mail: hyhe@ipe.ac.cn*
[b]*National Engineering Research Center of Chemical Fertilizer Catalyst, School of Chemical Engineering, Fuzhou University, Fuzhou 350002, Fujian, China. E-mail: jll@fzu.edu.cn*
[c]*University of Chinese Academy of Sciences, Beijing 100049, China*
†Electronic supplementary information (ESI) available. See DOI: 10.1039/d0gc03551c
‡Co-first author.

The most common linkages in lignin are β-1, β-5, 5–5, β–β, β-O-4, α-O-4, 4-O-5, *etc*. It has been found that lignin contains 75% and 25% of ether (C–O) and carbon–carbon (C–C) bonds, respectively,[3,4,7] in which the C–C bonds are much stronger than the C–O bonds. Thus, selective cleavage of C–O bonds allows maximum degradation of lignin while retaining its aromatic monomer structure. So far, the conversion of lignin into the building blocks for the chemical industry has been carried out by hydrolysis,[11,12] hydrogenolysis,[13,14] oxidation,[15–17] *etc*. These conventional processes usually require harsh conditions such as high temperature (>100 °C), high pressure of H_2 or O_2, toxic solvents, and so on. Therefore, the economic utilization of lignin still faces many challenges due to the high recalcitrance of its structure. Among all the reported technologies, those based on ionic liquids (ILs) are of particular interest.[4,6] ILs are a kind of green and reusable medium composed of organic cations and organic/inorganic anions with the advantages of a wide electrochemical window, non-volatility, high thermal stability, and nonflammability, as composed to the traditional organic solvents.[18–20,66] It has been revealed that ILs can form strong hydrogen bonds with lignocellulosic biomass molecules, resulting in excellent solubility of lignocellulose.[21,22] ILs can also be used as catalysts for lignocellulosic biomass processing.[4,23,24] Following the pioneering study by Rogers *et al.* on the biomass dissolution and treatment in ILs,[21] many homogeneous and heterogeneous transformations of lignin in ILs were extensively investigated due to the high selectivity and easy separation of the products.[25–27,67]

To realize the catalytic degradation of lignin and its model compounds in ILs, several different strategies have been investigated, such as acid/base catalytic hydrogenation, photocatalysis, electrocatalysis, *etc*.[4,6] Among them, electrocatalysis is the most promising and attractive method due to its mild and green operating conditions (ambient pressure and temperature in aqueous or less toxic solvents), avoidance of expensive noble metal catalysts, and potential for large-scale applications.[28–30] At present, the electrochemical degradation of lignin is mainly focused on direct oxidation using metal composites as anodes, such as Ti/Sb-SnO_2, Ti/PbO_2, Ti/Ta_2O_5-IrO_2, Ti/SnO_2-IrO_2, Ti/RuO_2-IrO_2, and Ti/TiO_2-IrO_2.[8,31] Recently, the indirect oxidation of lignin by using reactive oxygen species (ROSs) generated *in situ* at the electrode *via* the oxygen reduction reaction (ORR) is also gradually attracting extensive attention. This method has both economical and environmentally friendly advantages from several perspectives.[32,33] Firstly, the electrocatalytic degradation conditions are mild, and there is no need to heat, pressurize, or use expensive gases. The oxygen used in the reaction can be obtained from the atmosphere, effectively reducing the processing costs. Secondly, based on the anodic process and cathodic reduction process, the method significantly improves the treatment efficiency and reduces the side reactions through the rational design of the electrocatalytic setup, which is simple and practicable. Finally, many studies have shown that ROSs are a class of highly efficient, environmentally benign, and sustainable strong oxidizing reagents with potential application in various fields such as energy, environment, and the chemical industry. Specifically, the ROSs generated by reduction reaction that achieves the degradation of lignin and its model compounds are mainly composed of $^{\bullet}O_2^-$ and H_2O_2, which cleave the alkyl-O-aryl bonds in lignin and indirectly depolymerize lignin in aqueous solutions or IL electrolytes.[34–36] Besides, the stability of ROSs is very sensitive to the electrochemical environment.[37] For instance, the $^{\bullet}O_2^-$ radical is stable under anhydrous conditions, whereas it can react with ILs containing imidazolium and phosphonium cations, especially in the presence of protonic impurities,[38–40] which are easy to be protonated. Therefore, it can be expected that the protic ionic liquid is not only very effective in dissolving lignin, but also an ideal electrolyte in electrochemical depolymerization of lignin.[41,42,65]

Furthermore, the degradation and upgrading of lignin using electrochemical methods have been studied to some extent,[8,31] but how to efficiently and selectively cleave C–O bonds by electrocatalysis remains challenging. At present, evidence of intermediates produced during the electrocatalytic oxidation reaction of lignin and its derivatives is still insufficient, making it extremely difficult to reasonably understand the microscopic mechanism of a given reaction. Therefore, to better and more intuitively discuss the electrocatalytic cleavage reactions of C–O bonding of lignin and its derivatives, we choose four phenolic lignin model compounds, 4-ethoxyphenol (EP), 4-phenoxyphenol (PP), *p*-benzyloxyphenol (PBP) and 2-(2-phenylethoxy)phenol (2-PEP), with typical C–O bonds as substrates,[11,14] and use a protic IL [BSO_3Hmim][OTf] as the electrolyte, to explore the cleavage mechanism of the C–O bond. The electrochemical oxidation–reduction behaviors of these four phenolic lignin model compounds in [BSO_3Hmim][OTf]–H_2O are studied in detail. The effects of O_2

Hongyan He

Prof. Hongyan He received her Ph.D degree in applied chemistry from the Institute of Process Engineering (IPE), Chinese Academy of Sciences (CAS), in 2014. She was a visiting scholar at the University of Wyoming, working with Prof. Maohong Fan. She was elected as a member of the Youth Innovation Promotion Association of CAS in 2016 and received the CAS Science and Technology Promotion and Development Prize in 2017 and Houdebang Science and Technology Award for Young Talent in 2019. Her current research interests focus on (1) theoretical studies of the structure and properties of functionalized ionic liquids, including bulk phase and interfacial ionic liquids, and (2) fundamental investigations of lignin depolymerization and CO_2 conversion based on ionic liquids.

and H_2O on the degradation activity of the substrates are also investigated. Finally, the cleavage mechanism of the C–O bond is obtained by analyzing the degradation products of phenolic lignin model compounds, isotope labeling experiment, and the cyclic voltammetry (CV) curves of the substrates in the $[BSO_3Hmim][OTf]$–H_2O system.

2. Experimental

2.1 Chemicals and materials

4-Ethoxyphenol (EP, >99%), 4-phenoxyphenol (PP, >99%), *p*-benzyloxyphenol (PBP, >99%), 2-(2-phenylethoxy)phenol (2-PEP, >99%), phenol (>99%), *o*-hydroxyphenol (*o*-HP, >99%), benzyl alcohol (>99%), benzaldehyde (>99%), *p*-benzoquinone (*p*-BQ, >99%), phenethyl alcohol (>99%), ethanol and methanol (analytical grade, 99.99%) were obtained from Sinopharm Co. Ltd (Beijing, China). 1-Butylsulfonate-3-methylimidazolium trifluoromethanesulfonate ($[BSO_3Hmim][OTf]$) was purchased from Lanzhou Institute of Chemical Physics (Lanzhou, China) and dried at 45 °C under vacuum conditions for 48 h before use. Deionized (DI) water has an electrical resistivity of 18.2 MΩ cm and a conductivity of 1.18 μs cm^{-1}. The RuO_2-IrO_2/Ti mesh was provided by Northwest Institute for Non-ferrous Metals Research (Xi'an, China). Graphite felt was received from Yichang Beite Graphite New Material Co. Ltd (Yichang, China). The molecular structures of the four phenolic lignin model compounds and $[BSO_3Hmim][OTf]$ are provided in Scheme 1.

2.2 Electrochemical studies

The CV experiments were performed on an electrochemical workstation (CHI 660D, CH Instruments, Shanghai, China) using a three-electrode cell. A platinum wire (0.5 mm in diameter) and glassy carbon (GC) electrode (3 mm in diameter) were used as the counter and working electrodes, respectively. The Ag-quasi-reference electrode was fabricated by immersing a Ag-wire in a glass tube with a porous plug. The GC electrode was polished with aqueous slurries of 0.3 and 0.05 μm alumina, cleaned in an ultrasonic bath for 5 min, and then dried with N_2. The electrolyte was saturated with N_2 or O_2 before each experiment.

The electron transfer number of the ORR was determined using the rotating ring-disk electrode (RRDE) technique on an electrochemical workstation (CHI 760E, CH Instruments, Shanghai, China). The rotator (RRDE-3A) was purchased from ALS (Japan) Co., Ltd. A GC disk with a Pt ring (7 mm in diameter for the disk) was used as the rotating ring-disk working electrode. For the $[BSO_3Hmim][OTf]$ system, the disk potential was scanned from 0 to −0.6 V with a rate of 5 mV s^{-1} in O_2-saturated electrolyte, and the ring potential was maintained at 0.8 V. The rotating speed of the ring-disk electrode was maintained at 2000 rpm at room temperature. For the $[BSO_3Hmim][OTf]$–H_2O system, the disk potential was scanned from 0 to −0.8 V with a rate of 5 mV s^{-1} in O_2-saturated electrolyte, and the ring potential was maintained at 1.2 V. The rotating speed of the ring-disk was maintained at 1600 rpm at room temperature. Then the number of electron transfer (n) of the ORR was calculated by eqn (1).[43–45]

$$n = \frac{4I_d}{(I_r/N) + I_d} \quad (1)$$

where I_d is the disk current intensity, and I_r is the ring current intensity. N is the collection efficiency, determined to be 0.42 ± 0.01 in the case.

2.3 Electrolysis of phenolic lignin model compounds

The electrolysis of phenolic lignin model compounds was performed in a three-electrode cell using RuO_2-IrO_2/Ti mesh (20 mm × 20 mm) and graphite felt (20 mm × 20 mm) as the working electrode alternately. The typical procedure was the same as for the CV test. The concentration of the phenolic lignin model compounds was 20 mM in all electrolyte systems. The electrolysis experiments were conducted at room temperature under either an O_2 or N_2 atmosphere.

2.4 GC-MS and HPLC analysis

The degradation products were analyzed using a gas chromatograph plus mass spectrometer (GC-MS, Agilent 5977B) equipped with an HP-5MS Ultra Inert capillary column (30 m × 250 μm × 0.25 μm) and a 7697A headspace sampler. A 25 μL sample was first extracted at 170 °C in the headspace for 4 min and then tested at a split ratio of 10 : 1. The degradation products of PBP were analyzed with a Waters Xevo TQ high-performance liquid chromatograph (HPLC) equipped with a UV-detector and a C18 column (250 mm × 4.6 mm i.d., 5 μm) using a mixed solution of methanol and water (70 : 30, v/v) as the mobile phase at a flow rate of 0.4 mL min^{-1}. The observed products were quantified at 254 nm using an external standard method.

2.5 Computational methods

The solubility of O_2 in the solutions of IL–H_2O-phenolic lignin model compounds was analyzed using the Gaussian 09 software package[68] and the model COSMO-RS (implementation: COSMOtherm version C3.0 release 14.01, applied with parameterization BP_TZVP_C30_1401, COSMOlogic, Leverkusen, Germany). The stable geometries of $[BSO_3Hmim]^+$, $[OTf]^-$, H_2O, O_2, and phenolic lignin model compounds were optimized by using Gaussian 09 at the B3LYP/6-311+G(d,p) level of theory. The COSMO files of these compounds were calculated at the same theoretical level using the COSMO continuum solvation model. The O_2 solubility in various IL–H_2O-phenolic lignin model compound mixtures was determined by using the COSMO-RS program at 25 °C and 1.013 bar. The phenolic lignin model compound concentrations were kept at 20 mM in these mixtures, and the volume ratios of the IL to H_2O were 1 : 1, 2 : 1, and 4 : 1, respectively. Also, to determine the diffusion coefficients of O_2 and phenolic lignin model compounds in ILs, the Large-scale Atomic/Molecular Massively Parallel Simulator (LAMMPS) was applied to perform the simu-

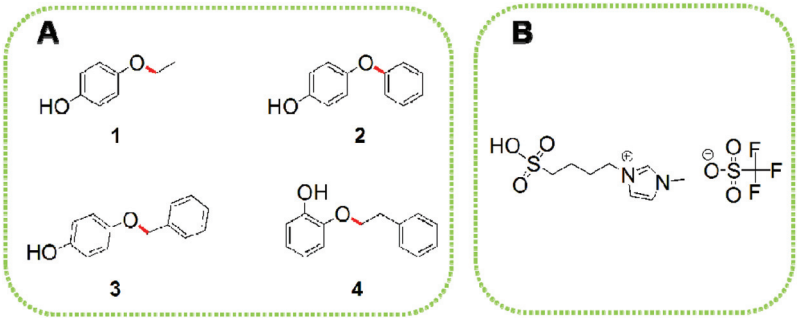

Scheme 1 Molecular structures of the four phenolic lignin model compounds (A) (1, EP; 2, PP; 3, PBP; 4, 2-PEP) and [BSO_3Hmim][OTf] (B).

lation. The interactions between O_2, [BSO_3Hmim][OTf], and phenolic lignin model compounds include both electrostatic and van der Waals terms. The former is a long-range coulombic interaction, computed by the particle–particle–particle–mesh (PPPM) algorithm. The latter was described using the 12-6 Lennard-Jones potential. The Lorentz-Berthelot mixing rules were used to model the parameters between different atomic species, which were truncated at 1.2 nm. The diffusion coefficient was calculated by statistical averaging over at least 5 independent simulations (see section 1 of the ESI† for the calculation details).

3. Results and discussion

3.1 Physical properties of [BSO_3Hmim][OTf] solutions

The conductivity of the studied systems and the diffusion coefficients of O_2 and the four phenolic lignin model compounds were obtained by simulations. Here, the PBP electrolysis system was taken as an example, and similar results of the other three electrolysis systems are shown in Fig. S1.† As shown in Table 1 and Fig. 1, the conductivity of the [BSO_3Hmim][OTf]–H_2O solution first decreases after the addition of water because water molecules induce the intermolecular interactions among IL molecules. With a further increase in water content, the conductivity of the solution system can be increased due to the abundant water molecules that increase the free migration of IL ions. The variation tendency of the solubility and diffusion coefficient of O_2 is similar to that of the conductivity. The oxygen molecules with small sizes may diffuse through the interstices among IL ions, while water molecules may change the microenvironment of ILs, resulting in the variation of the O_2 solubility. The diffusion coefficient of O_2 in these studied IL systems disobeys the Stokes–Einstein relationship due to the non-Stokesian behavior of glass former ILs.[46,47] As for the diffusion of PBP, D_{PBP} shows an increase with increasing water content because the addition of water sharply reduces the viscosity of the IL system,[48,49] inducing both an increase in D_{PBP} and an enhancement of the electrolyte mass transfer.

3.2 ORR in the [BSO_3Hmim][OTf]–H_2O system

Since ROSs generated by the ORR are critical for the depolymerization of lignin,[34–36] the CV experiments were carried out in both O_2 and N_2-saturated [BSO_3Hmim][OTf]–H_2O solutions (Fig. 2). As shown in Fig. 2, the CV curves (black line) do not display redox peaks under a N_2 atmosphere, indicating that the water and [BSO_3Hmim][OTf] have not been degraded and also showing the preferable stability of the [BSO_3Hmim][OTf] ionic liquid (related discussions can be seen in Sections 8 and 9 of the ESI†). A reduced peak associated with O_2 can be found in the CV curves under an O_2 atmosphere (marked as a), and the current value of this peak a increases with the increase of H_2O content, but this phenomenon is not observed under a N_2 atmosphere. In other words, this phenomenon indicates that both the O_2 concentration and the electrolyte's conductivity increase due to the reduced electrolyte viscosity and enhanced O_2 diffusion. The experiment data for these properties are con-

Table 1 The conductivity of different studied systems, the solubility of O_2 (C_O), and the diffusion coefficients of O_2 (D_O) and PBP (D_{PBP}) at room temperature

Entry	Conductivity[a] (μs cm^{-1})	C_O[b] (mmol L^{-1})	D_O[c] (m^2 s^{-1})	D_{PBP}[c] (m^2 s^{-1})
H_2O	1.18	0.26	2.5782×10^{-9}	—
[BSO_3Hmim][OTf]	379	0.90	1.7426×10^{-11}	2.3732×10^{-13}
[BSO_3Hmim][OTf]–H_2O (4 : 1, v : v)	18.94	1.36	8.1919×10^{-12}	6.6871×10^{-13}
[BSO_3Hmim][OTf]–H_2O (2 : 1, v : v)	64.4	1.19	8.0951×10^{-11}	5.3532×10^{-12}
[BSO_3Hmim][OTf]–H_2O (1 : 1, v : v)	143.4	0.85	3.3935×10^{-10}	2.1158×10^{-11}

[a] The conductivity of different systems was measured by using a Mettler conductivity meter. [b] The O_2 concentration in the four systems (pure IL, 4 : 1, 2 : 1, and 1 : 1) was calculated by COSMO-RS. [c] The diffusion coefficients of O_2 and the phenolic lignin model compound (PBP) were obtained by MD simulation.

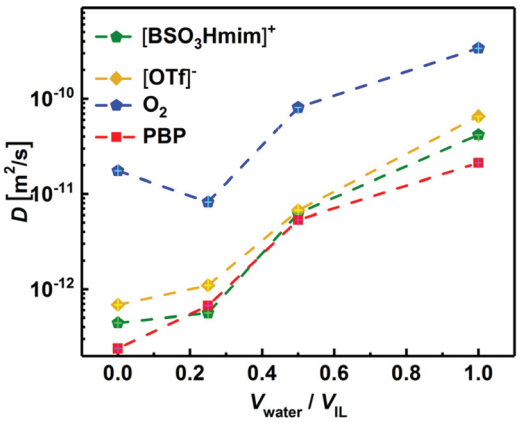

Fig. 1 The diffusion coefficients of $[BSO_3Hmim]^+$, $[OTf]^-$, O_2 and PBP.

sistent with MD simulation results except for the pure IL system (see Table 1). It is found that the transfer of O_2 to the electrode surface may be controlled by diffusion as the H_2O content increases. Then CV experiments were performed under an O_2 atmosphere at different scanning rates with the GC electrode, and the results verify the above viewpoint, as shown in Fig. S2.† In general, there are two products during the ORR in the presence of a protic IL or aqueous acid electrolyte. One is H_2O_2 *via* a two-electron reduction pathway, and the other is H_2O *via* a four-electron reduction pathway.[50] To further clarify whether the product in peak a is H_2O_2 or H_2O, we calculated the electron transfer numbers of the ORR in both pure $[BSO_3Hmim][OTf]$ and $[BSO_3Hmim][OTf]$–H_2O mixtures by RRDE results.

Fig. 3shows the current density (A and C) and electron transfer numbers (B and D) of the ORR process. The results demonstrate that the ORR electron transfer numbers in $[BSO_3Hmim][OTf]$ (at −0.372 V, see Fig. 2A) and $[BSO_3Hmim][OTf]$–H_2O (2 : 1, at −0.565 V, see Fig. 2C) are 2.18 and 2.53, respectively, indicating the formation of H_2O_2 through a two-electron transfer process during the ORR. Thus, it can be speculated that the ORR process in ILs may follow the electrochemical–chemical–electrochemical–chemical (ECEC) mechanism,[46] as described in eqn (2)–(5).

$$O_2 + e \leftrightarrow {}^{\bullet}O_2^- \quad (2)$$

$${}^{\bullet}O_2^- + H^+ \leftrightarrow {}^{\bullet}HO_2 \quad (3)$$

$${}^{\bullet}HO_2 + e \leftrightarrow HO_2^- \quad (4)$$

$$HO_2^- + H^+ \leftrightarrow H_2O_2 \quad (5)$$

3.3 Electrochemical behavior of phenolic lignin model compounds in the $[BSO_3Hmim][OTf]$–H_2O system

The electrochemical behavior of the phenolic lignin model compound PBP in the $[BSO_3Hmim][OTf]$–H_2O electrolyte is first measured, and the results are shown in Fig. 4. Under an O_2 atmosphere, four peaks appear in all CV curves, labeled as a, 3b, 3c, and 3d, respectively, where a and 3b represent the reduction peaks, and 3c and 3d are the oxidation peaks. In contrast, only three peaks are observed under a N_2 atmosphere, indicating that peak a can be attributed to the reduction of O_2. This result is consistent with the results shown in Section 3.2. Meanwhile, with the increase of H_2O content, the area and current values of peak 3c increase continuously, which can be attributed to the decrease of the viscosity of $[BSO_3Hmim][OTf]$.

Further, we performed a segment-by-segment analysis of the electrochemical behavior of the phenolic lignin model

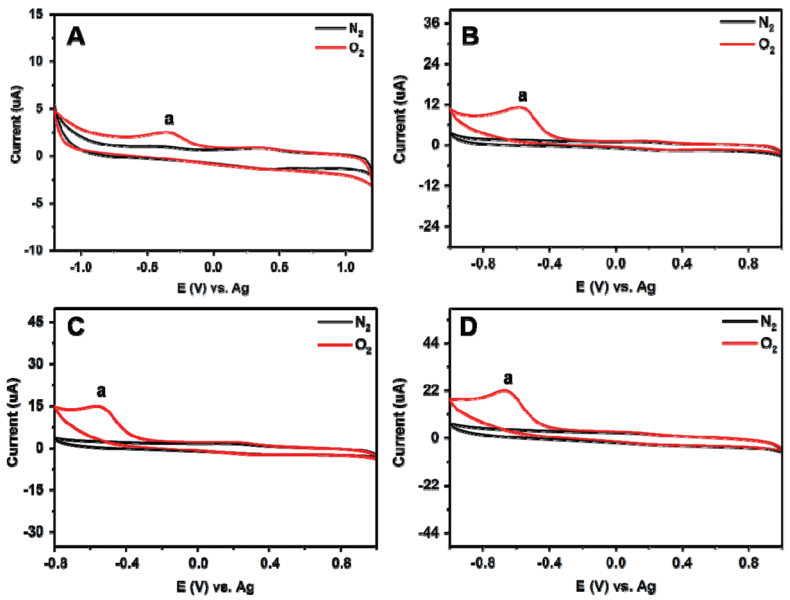

Fig. 2 CV curves recorded on the GC electrode in pure $[BSO_3Hmim][OTf]$ (A) and $[BSO_3Hmim][OTf]$–H_2O with the volume ratios of 4 : 1 (B), 2 : 1 (C), and 1 : 1 (D) under both O_2 and N_2 atmospheres with a scanning rate of 50 mV s^{-1} at room temperature.

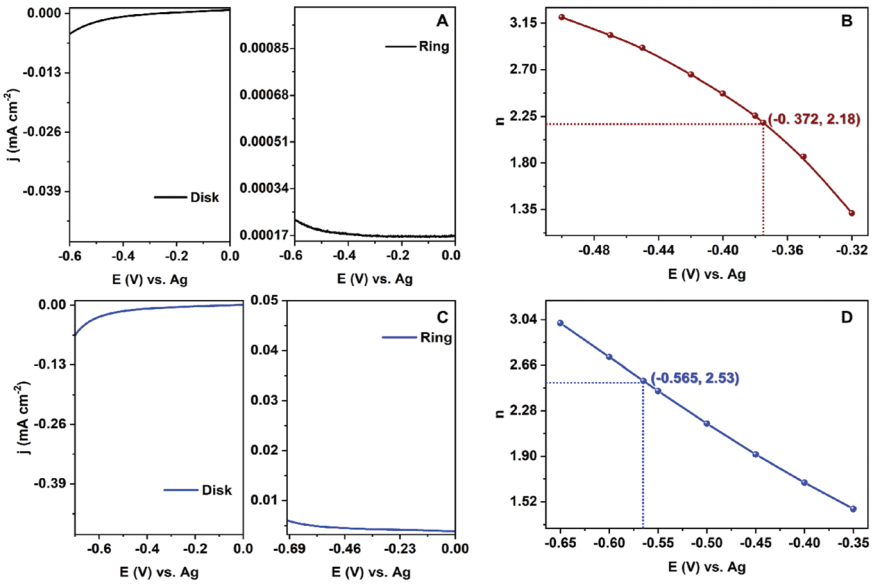

Fig. 3 *I–V* curves of the RRDE and electron transfer numbers in different systems. (A) and (C) are the *I–V* curves of the RRDE in [BSO_3Hmim][OTf] or [BSO_3Hmim][OTf]–H_2O (2 : 1) at 2000 and 1600 rpm, respectively, and the corresponding ring current recorded at a Pt ring potential of 0.8 and 1.2 V, respectively. (B) and (D) are the calculated electron transfer numbers of the ORR from the RRDE curves in (A) and (C).

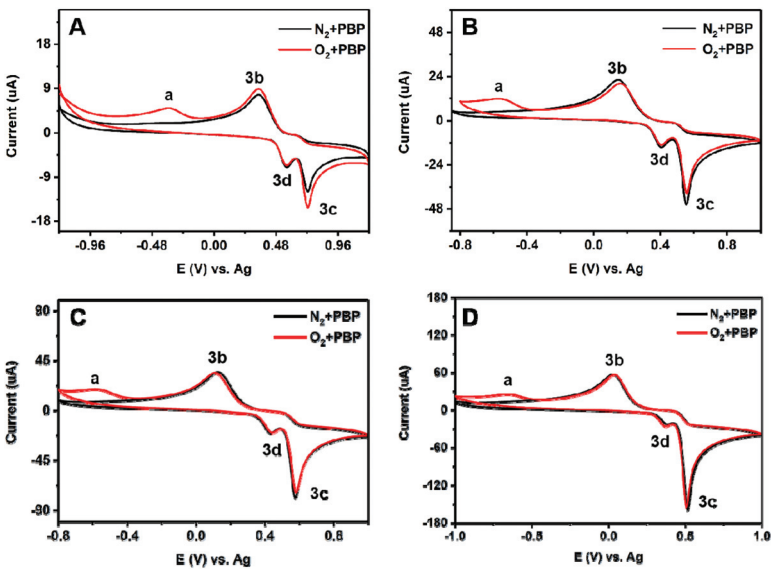

Fig. 4 CV curves recorded on the GC electrode in pure [BSO_3Hmim][OTf] (A) and [BSO_3Hmim][OTf]–H_2O with the volume ratios of 4 : 1 (B), 2 : 1 (C) and 1 : 1 (D) under both O_2 and N_2 atmospheres with a scanning rate of 50 mV s^{-1} at room temperature. The concentration of PBP in all the electrolytes is 10 mM.

compound PBP under a N_2 atmosphere and determined the peaks of 3b, 3c, and 3d (for detailed analysis of the electrochemical behavior of the other three model compounds, refer to Section 4 of ESI†). As shown in Fig. 5, the potential is swept negatively from the open circuit potential to about −1.0 V, and there is no peak in the 1st segment. And then, the oxidation peak 3c and the reduction peak 3b appear in the 2nd and 3rd segments, respectively. At the same time, two oxidation peaks (3c and 3d) arose in the 4th segment. Thus, we can speculate that peak 3c is the oxidation peak of PBP, while the newly appeared peak 3d in the 4th segment may be the oxidation peak of the degradation products of PBP on the electrode. We know that phenols with hydroxyl (–OH) functional groups are readily oxidized.[51,52] Therefore, these compounds can act as antioxidants, scavenging free radicals by H-atom or electron transfer processes and subsequently converting phenols to phenoxy radicals.[53] Thus, PBP may be oxidized to phenoxyl or quinone radicals in oxidation peak 3c.[54] In the 3rd segment,

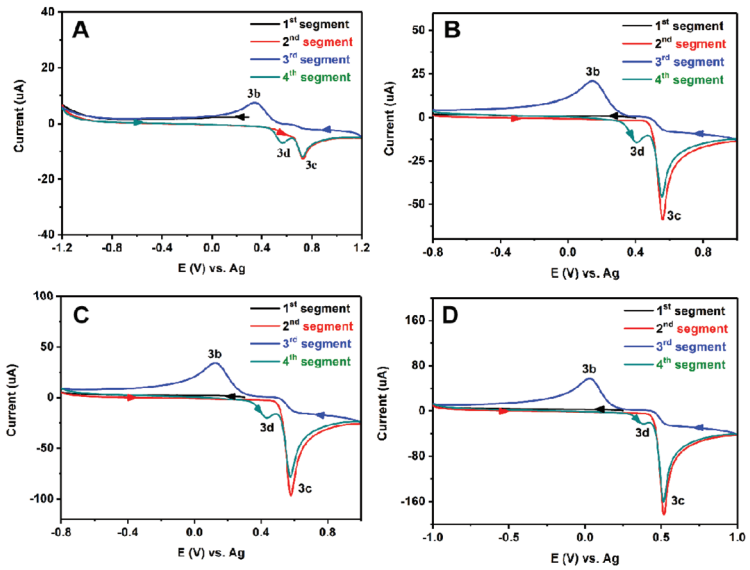

Fig. 5 CV curves recorded on the GC electrode in pure [BSO_3Hmim][OTf] (A) and [BSO_3Hmim][OTf]–H_2O with the volume ratios of 4 : 1 (B), 2 : 1 (C) and 1 : 1 (D), containing 10 mM PBP under a N_2 atmosphere at room temperature. Scan rate: 50 mV s^{-1}.

the potential of the GC electrode is swept from 1.0 to −1.0 V at 50 mV s^{-1}, which ensures that all electrogenerated quinone-based compounds could be reduced to phenolic hydroxyl at a given voltage and the redox mechanism is illustrated in Scheme S2 in the ESI.† The oxidation–reduction reaction of PBP on the GC electrode is similar to that reported previously.[35,44] During the redox cycling, PBP can be converted into *p*-BQ (or hydroquinone), benzyl alcohol, and benzaldehyde. Among them, the electrocatalytic oxidation–reduction of *p*-BQ (or hydroquinone) occurs more readily, resulting in reversible conversion between them.[55] Therefore, to confirm this speculation, we further carried out the electrochemical reduction–oxidation reaction of *p*-BQ under a N_2 atmosphere (Fig. 6). Firstly, when the potential is scanned forward from the open circuit potential to about 1.0 V, *p*-BQ is reduced to hydroquinone (peak e), and then the resulting hydroquinone is oxidized to *p*-BQ (peak f). It is noteworthy that the potentials of peaks 3d and f are almost equal. So, the oxidation peak 3d is related to hydroquinone oxidation, as shown in Fig. S3A and Scheme S1A.† As for the reduction peak e, it overlaps with the peak 3b. This confirms the reduction of *p*-BQ in peak 3b. However, the peak area of 3b is much larger than that of 3d (Fig. 6). Another reduction of quinone may also occur simultaneously in peak 3b, which may be from the oxidation state of PBP (Scheme S2 in the ESI†). Based on the CV results, we can also conclude that PBP molecules undergo electrocatalytic degradation in the IL–H_2O systems.

3.4 Effect of H_2O on the degradation of phenolic lignin model compounds

Based on the above results, we know that the composition of [BSO_3Hmim][OTf]–H_2O (*e.g.*, 2 : 1 and 1 : 1) has higher saturated concentrations and diffusion coefficients of O_2 and phenolic lignin model compounds. Considering that kinetics is a vital issue for the degradation effect, we further determined the degradation percentage of phenolic lignin model compounds (continuing with PBP degradation as an example) in [BSO_3Hmim][OTf] with different H_2O contents. As shown in Fig. 7, the degradation percentage of PBP increases as the H_2O content in the [BSO_3Hmim][OTf] electrolyte increases. In particular, after 8 hours, the degradation percentage of PBP in both [BSO_3Hmim][OTf]–H_2O (2 : 1) and [BSO_3Hmim][OTf]–H_2O (1 : 1) (curves c and d) is close to 100%, which is approximately 2 times higher than that in pure [BSO_3Hmim][OTf]. To have more insights into the reaction kinetics, we calculated the initial degradation rate (ν_0) of PBP in these four systems (Fig. 7B). The ν_0 of PBP in these four systems is about 0.0127, 0.0738, 0.1677, and 0.2571 mmol (L min)$^{-1}$, respectively, indicating that ν_0 increases rapidly with the increase of H_2O content. When the volume ratio of [BSO_3Hmim][OTf] to H_2O is 2 : 1 and 1 : 1, ν_0 is one order of magnitude faster than that in pure [BSO_3Hmim][OTf]. The results show that the H_2O content has a significant influence on the electrolysis reaction, *e.g.*, decreasing the electrolyte's viscosity and enhancing the mass transfer capacity and conductivity of the solution.[56] The results are consistent with the D_{PBP} data in Table 1. Besides, the degradation percentages of PBP in H_2O, pure [BSO_3Hmim][OTf], and [BSO_3Hmim][OTf]–H_2O systems were also compared (Fig. S6†), showing that the IL–H_2O system is more favorable for the electrocatalytic degradation of the substrate. A more detailed discussion can be found in Section 6 of ESI.† Considering the high electrocatalytic activity in [BSO_3Hmim][OTf]–H_2O (2 : 1), we chose this system for further study and used it as the electrolyte for the electrochemical degradation of the other three model compounds.

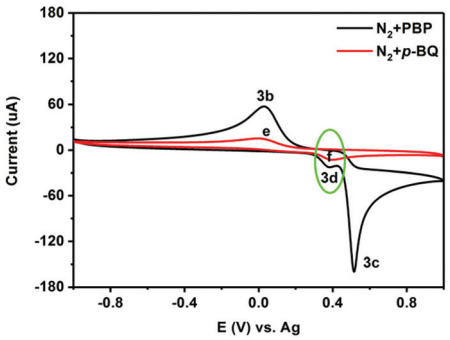

Fig. 6 CV curves recorded on the GC electrode in [BSO_3Hmim][OTf]–H_2O (1 : 1) containing 10 mM PBP (black), compared with 1 mM *p*-BQ (red) in the same electrolyte under a N_2 atmosphere at room temperature. Scan rate: 50 mV s^{-1}.

3.5 Electrolysis of phenolic lignin model compounds at different working electrodes and its products

The phenolic lignin model compounds were electrolyzed in the [BSO_3Hmim][OTf]–H_2O (2 : 1) system, and it was found that the O_2 atmosphere is more favorable for this process. To better understand the phenomenon, the degradation of PBP was conducted in a three-electrode cell, in which RuO_2-IrO_2/Ti mesh and graphite felt were used as the working electrode alternately, and the other one was as the counter electrode. When graphite felt was used as the working electrode (Fig. 8B) with an applied potential of −0.6 V, the ORR would occur on the graphite felt electrode under an O_2 atmosphere to form H_2O_2. The corresponding oxidation reaction of PBP occurs on the counter electrode (RuO_2-IrO_2/Ti mesh). Here, we define the oxidation of PBP on the electrode as a direct oxidation reaction. When the above catalytic reactions were carried out under a N_2 atmosphere, PBP is still directly oxidized on the RuO_2-IrO_2/Ti mesh electrode, but no H_2O_2 is generated. Combined with the result that the catalytic activity of PBP under O_2 is higher than that under N_2 (Fig. 8A), it can be concluded that H_2O_2 can also indirectly oxidize PBP. To further clarify this assumption, we used RuO_2-IrO_2/Ti mesh as the working electrode (Fig. 8D) and the graphite felt as the counter electrode, at an applied potential of 0.6 V, which resulted in similar results to those in Fig. 8A, as shown in Fig. 8C. It is verified that the PBP degradation under an O_2 atmosphere contains both direct and indirect means. Thus, PBP can be directly oxidized on the RuO_2-IrO_2/Ti mesh electrode under both O_2 and N_2 atmospheres, while indirect oxidation of the ORR can only be conducted under an O_2 atmosphere.

In order to further confirm the contribution of direct and indirect oxidation to this process, we conducted a kinetic study of the PBP degradation process, and the detailed results are shown in Fig. S7.† It can be found that although the working electrodes are different, the kinetic results are similar. Comparing the data in Fig. S7,† we noticed that the initial rate (v_0) under an O_2 atmosphere is higher than that under a N_2 atmosphere, further indicating that PBP undergoes both direct oxidation and indirect oxidation by *in situ* generated H_2O_2 under an O_2 atmosphere and direct oxidation only under a N_2 atmosphere. Comparing the specific data in Fig. S7A and 7B,† it is evident that the contribution of indirect oxidation is not significant, indicating that the direct oxidation of PBP is dominant in the whole process.

Moreover, the RuO_2-IrO_2/Ti electrode, a typical dimensionally stable anode (DSA), has been reported to be widely used in the oxidation of organic compounds and degradation of stubborn phenolic compounds due to its good stability and few side effects.[57,58] That is why the RuO_2-IrO_2/Ti electrode in this study has excellent performance for the electrochemical oxidation of PBP. Based on these results, we carried out the electrolysis experiments of the other three lignin model compounds, *i.e.* EP, BP, and 2-PEP, in the [BSO_3Hmim][OTf]–H_2O (2 : 1) system at a constant voltage using the RuO_2-IrO_2/Ti electrode as the working electrode. The experimental results and discussion are presented later in Section 3.7.

The products of PBP degradation were analyzed by GC-MS (Fig. S11 and S12†), and the product distribution of PBP degradation is shown in Fig. 9. When RuO_2-IrO_2/Ti mesh is used as the working electrode, the main products are *p*-BQ (1), benzyl alcohol (2), and only trace amounts of benzaldehyde (3) (Fig. S11A and 11B†). In contrast, using graphite felt, the main products of PBP are *p*-BQ (1), benzyl alcohol (2), and benzaldehyde (3) (Fig. S11C and 11D†). Benzaldehyde most likely originates from the oxidation of benzyl alcohol.[59,60] It is note-

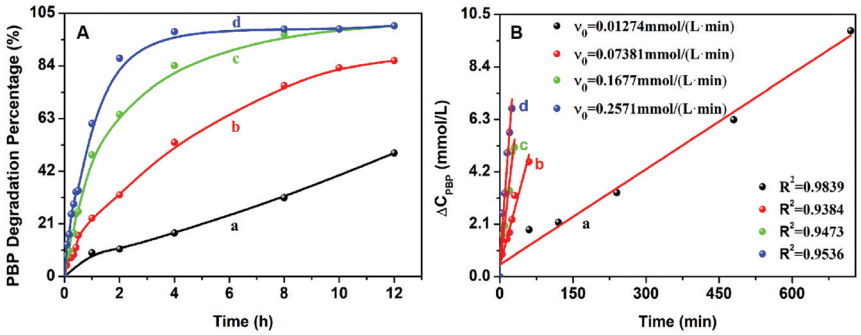

Fig. 7 (A) The degradation reaction of PBP in different electrocatalysis systems and (B) their corresponding initial reaction rate. Conditions: 20 mM PBP, under an O_2 atmosphere at room temperature. a, [BSO_3Hmim][OTf]; b, [BSO_3Hmim][OTf]–H_2O (4 : 1); c, [BSO_3Hmim][OTf]–H_2O (2 : 1) and d, [BSO_3Hmim][OTf]–H_2O (1 : 1).

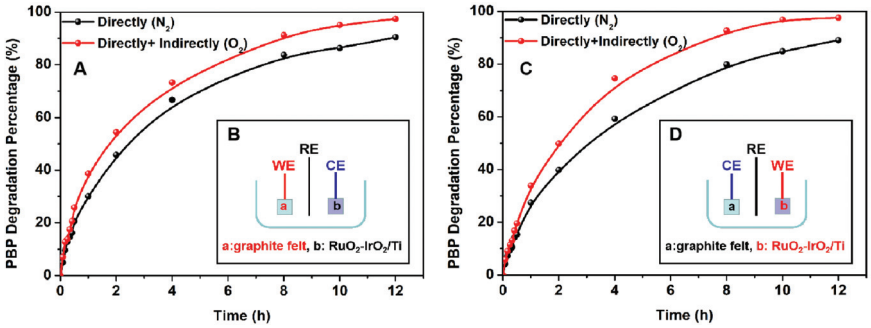

Fig. 8 The degradation percentage of PBP in the presence and absence of O_2. (A) and (C) are the reaction progress curves of PBP degradation under both O_2 (red line) and N_2 (black line) atmospheres. (B) and (D) show the placement of the three-electrode degradation cell, where graphite felt (at −0.6 V) and RuO_2-IrO_2/Ti (at 0.6 V) mesh were used as the working electrode alternately. Conditions: 20 mM PBP, room temperature, [BSO_3Hmim][OTf]–H_2O (2 : 1).

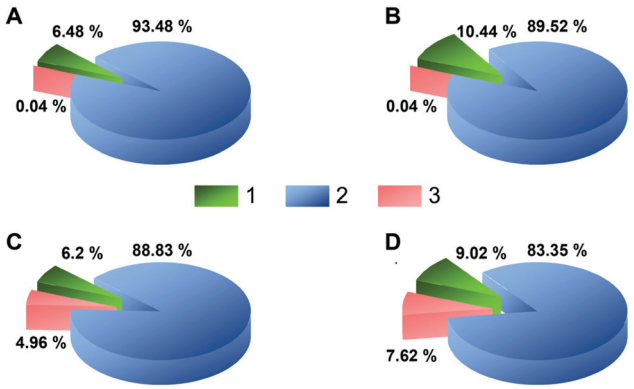

Fig. 9 Product distribution of PBP degradation on RuO_2-IrO_2/Ti mesh (A and B) and graphite felt (C and D) as working electrodes under N_2 (A and C) and O_2 (B and D) at an applied potential of 0.6 V and −0.6 V, respectively. Product: *p*-BQ (1), benzyl alcohol (2), and benzaldehyde (3). Conditions: 20 mM PBP, volume ratio of [BSO_3Hmim][OTf]–H_2O 2 : 1, room temperature, and reaction time 12 h.

worthy that the content of benzyl alcohol (2) is much higher than that of *p*-BQ on both the RuO_2-IrO_2/Ti mesh and graphite felt as the working electrodes. This may be due to the fact that *p*-BQ can be oxidized and mineralized on the anode into small molecular compounds such as lower aliphatic acids, CO_2, *etc.*[61,62] The product distribution results at different reaction times also provide strong evidence for this (Fig. S13 and S14†). Furthermore, we can also note that the product distributes very similarly under N_2 and O_2 on RuO_2-IrO_2/Ti mesh. However, the *p*-BQ content in the N_2-saturated electrolyte is lower than that under an O_2 atmosphere, regardless of whether graphite felt or RuO_2-IrO_2/Ti mesh is used as the working electrode, indicating that PBP oxidation under an O_2 atmosphere is driven by both direct and indirect ways, resulting in a higher content of *p*-BQ. Overall, the electrochemical degradation process of PBP is complicated, and the degradation mechanisms on the graphite felt and RuO_2-IrO_2/Ti electrodes may be different.

3.6 Possible mechanism of electrocatalytic cleavage of aromatic ether bonds

Based on the above results and discussion, the electrochemical degradation mechanism of PBP in the [BSO_3Hmim][OTf]–H_2O solution is proposed (Scheme 2). First, PBP molecules dissociate in the electrolyte, releasing a proton to form phenoxy anions (PBP^-), which then diffuses to the anode, where it donates an electron to generate the phenoxy radicals ($PBP_1^{\bullet}$) (peak 3c in Fig. 6). In the subsequent reverse scan, $PBP_1^{\bullet}$ recovers to PBP at an appropriate potential (peak 3b in Fig. 6). Then, $PBP_1^{\bullet}$ may transform into $PBP_2^{\bullet}$ through the quinone resonance, leading to the activation of the 2-C or 4-C atom (see Scheme 2).[54] This C atom might be the active site for the subsequent bond cleavage reactions.[35,36] Simultaneously, $PBP_2^{\bullet}$ may react with ROSs generated during the ORR process, leading to the indirect cleavage of the ether bond in $PBP_2^{\bullet}$ (pathway A in Scheme 2).[34,44] Moreover, PBP can also be degraded on the RuO_2-IrO_2/Ti electrode under a N_2 atmosphere (Fig. S11A†). Combining the results of Section 3.3 with those of Section 3.5, the electrochemical degradation mechanism of PBP on the RuO_2-IrO_2/Ti electrode under a N_2 atmosphere may be described as follows: the O on the ether bond ($PBP_2^{\bullet}$) may possess the alkaline property and readily binds to a proton to produce the oxonium ion, leading to the cleavage of the ether bond and formation of products, such as *p*-BQ (1), benzyl alcohol (2) and benzaldehyde (3) (pathway B in Scheme 2). Through pathway B, carbonium ions (intermediate product 4) are then attacked by H_2O to produce benzyl alcohol (2).[63,64] Subsequently, the benzyl alcohol can be further oxidized to benzaldehyde by oxidative dehydrogenation. To further verify the mechanism of pathway B, the oxygen isotope labeling experiment for PBP degradation was performed with RuO_2-IrO_2/Ti mesh as the working electrode under a N_2 atmosphere (using $H_2{}^{18}O$ instead of H_2O), and the mass spectrum of benzyl alcohol is shown in Fig. S15.† When H_2O and $H_2{}^{18}O$ were added to the electrolysis system, the mass-to-charge ratios of benzyl alcohol are 108 and 110, respectively, which means that the carbonium ion is combined with the hydroxyl group of H_2O to form benzyl alcohol (2).

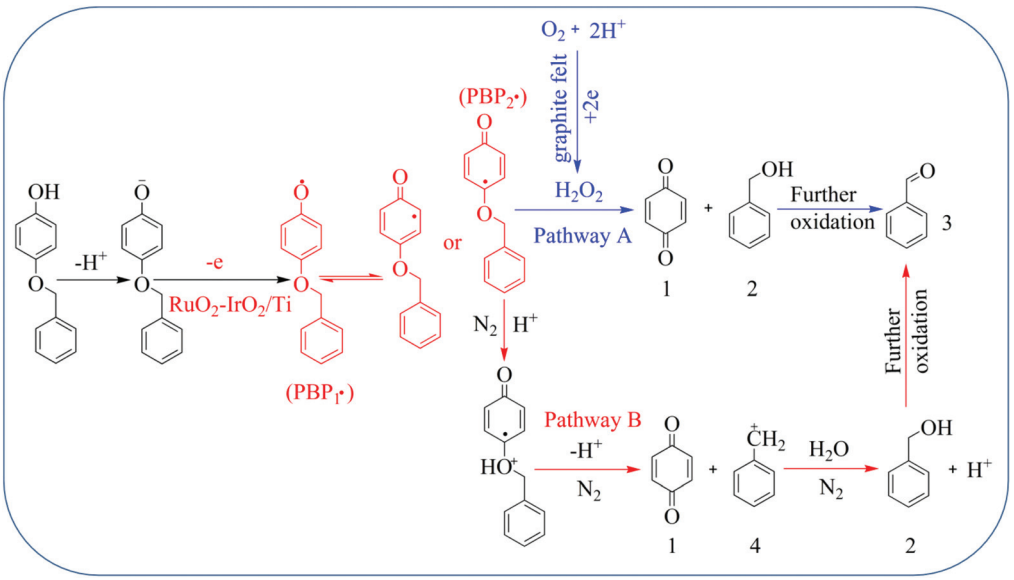

Scheme 2 The mechanism of electrochemical degradation of PBP in $[BSO_3Hmim][OTf]–H_2O$ solution *via* direct (pathway B) and indirect oxidation (pathway A).

3.7 Verification of the mechanism of electrocatalytic cleavage of aromatic ether bonds

In order to verify the above-proposed mechanism of electrocatalytic cleavage of aromatic ether bonds, the electrochemical behavior, degradation percentage, and degradation product distribution of the other phenolic lignin model compounds EP (**1**), PP (**2**), and 2-PEP (**4**) in the $[BSO_3Hmim][OTf]–H_2O$ (2 : 1) system, which are structurally similar to PBP, were further investigated, and the results are shown in Fig. 10. It can be observed that the CV curves of EP, PP, and 2-PEP under a N_2 atmosphere are very similar to those of PBP (Fig. 10A–C).

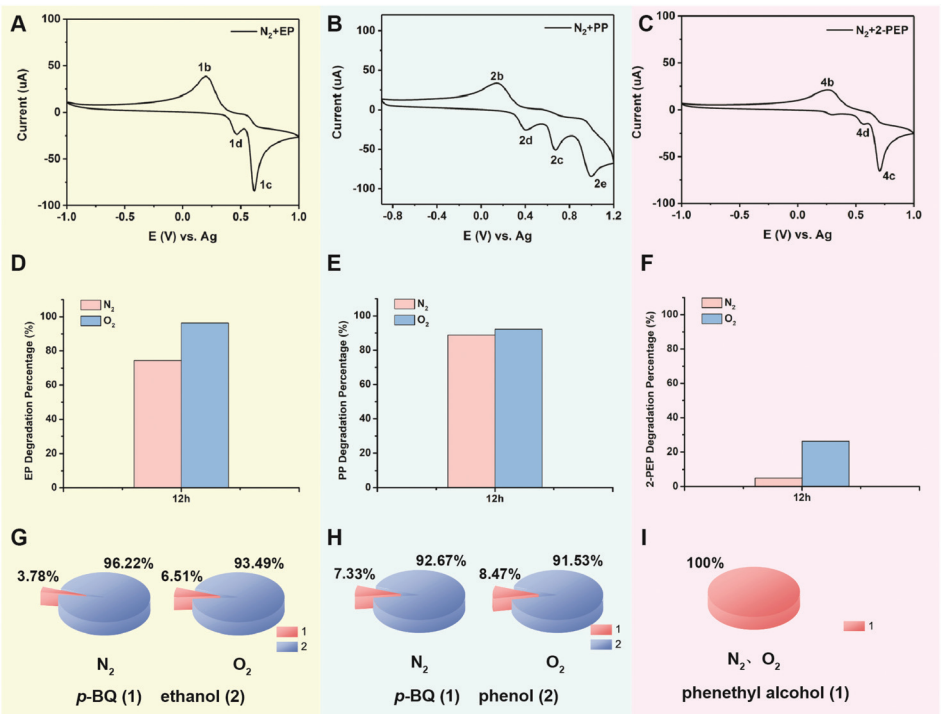

Fig. 10 Verification of the mechanism of electrocatalytic cleavage of ether bonds with different substrates. A, B and C are the CV curves of EP, PP and 2-PEP; D, E and F are the degradation percentages of EP, PP and 2-PEP; G, H and I are the degradation product distributions of EP, PP and 2-PEP. Conditions: RuO_2-IrO_2/Ti mesh used as the working electrode, 20 mM substrates, room temperature, $[BSO_3Hmim][OTf]–H_2O$ (2 : 1).

Specifically, the CV curves of EP and 2-PEP have two oxidation peaks (1c, 1d and 4c, 4d) and one reduction peak (1b and 4b), whereas PP has three oxidation peaks (2c, 2d and 2e) and one reduction peak (2b). Besides, it can be derived that the oxidation voltages of EP, PP, and 2-PEP are 0.62 (1c), 0.75 (2c), and 0.71 V (4c), respectively, and the corresponding peaks of the CV curves are given in Section 4 of ESI.† The oxidation voltages of PP and 2-PEP are higher than those of the other two substrates, which may be due to their substituents, substitution sites, and steric hindrance.

Then, the three phenolic lignin model compounds are degraded in the $[BSO_3Hmim][OTf]$–H_2O (2 : 1) system using the corresponding voltages, and the results are shown in Fig. 10D–F. It can be seen that the degradation percentages of these three substrates are higher under an O_2 atmosphere than those under a N_2 atmosphere, mainly due to the coupling of direct and indirect oxidation, as explained in Section 3.5, as well as the mechanism which can be referred to in Schemes S3 and S4.† EP and PP are degraded to produce *p*-BQ and the corresponding hydroxyl compounds (Fig. 10G and H; Fig. S16 and 18†). The hydroxyl compounds can be detected in the degradation products of all phenolic lignin model compounds, indicating that the substrate's C–O bond has been split to produce carbonium ions, which are then attacked by H_2O to produce the corresponding hydroxyl compounds. The reason for the formation of hydroxyl compounds is also demonstrated in Section 3.6. For the degradation of 2-PEP, the CV curves are similar to those of EP, PP, and PBP, indicating that such a phenolic lignin model compound can also be degraded, and its degradation mechanism can be referred to in Scheme S5.† However, the degradation percentage of 2-PEP is far lower than that of the other three substrates, and its degradation could be significantly promoted under an O_2 atmosphere, possibly because the ether bond activity of the *ortho*-position is lower than that of the *para*-position. Moreover, only one primary product, phenethyl alcohol, is detected, with no corresponding *o*-HP or 1,2-benzoquinone (Fig. 10L and Fig. S20†). This may be due to the fact that 1,2-benzoquinone is extremely unstable and could be oxidized and mineralized on the anode into small molecular compounds such as lower aliphatic acids, CO_2, *etc.*[61,62] These results tentatively validate the reasonability of the electrocatalytic cleavage of aromatic ether bonds in the $[BSO_3Hmim][OTf]$–H_2O (2 : 1) system.

4. Conclusions

In summary, the mild cleavage of C_{aryl}–O bonds is achieved by constructing an electrocatalytic oxidation system of four phenolic lignin model compounds with typical C–O bonds in a protic ionic liquid–H_2O electrolyte. The results indicate that the addition of H_2O can reduce the viscosity of the IL electrolyte system and thus improve its conductivity, while enhancing the diffusion of O_2 and phenolic lignin model compounds in it, which is beneficial to the degradation of the lignin substrates during the electrocatalytic process. Combined with the analysis of the electrochemical oxidation–reduction behavior of the lignin substrates and their degradation products, the electrochemical breaking mechanism of the C–O bond can be demonstrated, *i.e.*, the direct oxidation of the substrates at the electrode and the indirect oxidation by *in situ* generation of H_2O_2, in which the direct oxidation is dominant. The above findings may provide fundamental insights into the electrocatalytic conversion and depolymerization process of lignin and its derivatives.

Conflicts of interest

There are no conflicts to declare.

Acknowledgements

This work was supported by the Natural Science Foundation of Beijing Municipality (2182068), National Science Fund for Excellent Young Scholars of China (21922813), National Natural Science Foundation of China (21736003, 21921005 and 21878314), and the Youth Innovation Promotion Association of the Chinese Academy of Sciences (2017066). The authors sincerely appreciate Prof. Suojiang Zhang (IPE, CAS) for his careful academic guidance and great support.

References

1 A. J. Ragauskas, C. K. Williams, B. H. Davison, G. Britovsek, J. Cairney, C. A. Eckert, W. J. Frederick, J. P. Hallett, D. J. Leak, C. L. Liotta, J. R. Mielenz, R. Murphy, R. Templer and T. Tschaplinski, *Science*, 2006, **311**, 484–489.
2 G. W. Huber, S. Iborra and A. Corma, *Chem. Rev.*, 2006, **106**, 4044–4098.
3 B. M. Upton and A. M. Kasko, *Chem. Rev.*, 2016, **116**, 2275–2306.
4 Z. R. Zhang, J. L. Song and B. X. Han, *Chem. Rev.*, 2017, **117**, 6834–6880.
5 L. H. Hu, H. Pan, Y. H. Zhou and M. Zhang, *BioResources*, 2011, **6**, 3515–3525.
6 G. Y. Liu, Q. Wang, Y. Q. Zhang, H. Y. He and L. L. Jiang, *Sci. Sin.: Chim.*, 2020, **50**, 259–270.
7 Y. Q. Zhang, H. Y. He, Y. R. Liu, Y. L. Wang, F. Huo, M. H. Fan, H. Adidharma, X. H. Li and S. J. Zhang, *Green Chem.*, 2019, **21**, 9–35.
8 C. Z. Li, X. C. Zhao, A. Q. Wang, G. W. Huber and T. Zhang, *Chem. Rev.*, 2015, **115**, 11559–11624.
9 Y. T. Zhu, Z. J. Li and J. Z. Chen, *Green Energy Environ.*, 2019, **4**, 210–244.
10 A. Das, A. Rahimi, A. Ulbrich, M. Alherech, A. H. Motagamwala, A. Bhalla, L. da Costa Sousa, V. Balan, J. A. Dumesic, E. L. Hegg, B. E. Dale, J. Ralph, J. J. Coon and S. S. Stahl, *ACS Sustainable Chem. Eng.*, 2018, **6**, 3367–3374.

11 J. Zakzeski, P. C. A. Bruijnincx, A. L. Jongerius and B. M. Weckhuysen, *Chem. Rev.*, 2010, **110**, 3552–3599.
12 W. Schutyser, T. Renders, S. Van den Bosch, S. F. Koelewijn, G. Beckham and B. F. Sels, *Chem. Soc. Rev.*, 2018, **47**, 852–908.
13 C. F. Carrozza, G. Papa, A. Citterio, R. Sebastiano, B. A. Simmons and S. Singh, *Bioresour. Technol.*, 2019, **294**, 122214–122223.
14 Q. L. Song, Y. P. Zhao, F. P. Wu, G. S. Li, X. Fan, R. Y. Wang, J. P. Cao and X. Y. Wei, *Renewable Energy*, 2020, **148**, 729–738.
15 T. Vangeel, W. Schutyser, T. Renders and B. F. Sels, *Top. Curr. Chem.*, 2018, **376**, 30–45.
16 R. Behling, S. Valange and G. Chatel, *Green Chem.*, 2016, **18**, 1839–1854.
17 V. I. Pârvulescu and C. Hardacre, *Chem. Rev.*, 2007, **107**, 2615–2665.
18 L. Liang, J. P. Yan, Q. He, T. Luong, T. R. Pray, B. A. Simmons and N. Sun, *Green Energy Environ.*, 2019, **4**, 432–438.
19 H. Olivier-Bourbigou, L. Magna and D. Morvan, *Appl. Catal., A*, 2010, **373**, 1–56.
20 H. H. Zhang, M. Y. Zhu, W. Zhao, S. Li and G. Feng, *Green Energy Environ.*, 2018, **3**, 120–128.
21 R. P. Swatloski, S. K. Spear, J. D. Holbrey and R. D. Rogers, *J. Am. Chem. Soc.*, 2002, **124**, 4974–4975.
22 M. M. Hossain and L. Aldous, *Aust. J. Chem.*, 2012, **65**, 1465–1477.
23 A. Podgoršek, J. Jacquemin, A. A. H. Pádua and M. F. Costa Gomes, *Chem. Rev.*, 2016, **116**, 6075–6106.
24 J. P. Hallett and T. Welton, *Chem. Rev.*, 2011, **111**, 3508–3576.
25 D. Shao, J. D. Liang, X. M. Cui, H. Xu and W. Yan, *Chem. Eng. J.*, 2014, **244**, 288–295.
26 Z. P. Cai, J. X. Long, Y. W. Li, L. Ye, B. L. Yin, L. J. France, J. C. Dong, L. R. Zheng, H. Y. He, S. J. Liu, S. C. E. Tsang and X. H. Li, *Chem*, 2019, **5**, 2365–2377.
27 Z. M. Li, Z. P. Cai, Q. Zeng, T. Zhang, L. J. France, C. H. Song, Y. Q. Zhang, H. Y. He, L. L. Jiang, J. X. Long and X. H. Li, *Green Chem.*, 2018, **20**, 3743–3752.
28 D. Di Marino, V. Aniko, A. Stocco, S. Kriescher and M. Wessling, *Green Chem.*, 2017, **19**, 4778–4784.
29 P. Cai, H. X. Fan, S. Cao, J. Qi, S. M. Zhang and G. Li, *Electrochim. Acta*, 2018, **264**, 128–139.
30 S. Stiefel, J. Lölsberg, L. Kipshagen, R. Möller-Gulland and M. Wessling, *Electrochem. Commun.*, 2015, **61**, 49–52.
31 H. B. Zhu, L. Wang, Y. M. Chen, G. Y. Li, H. Li, Y. Tang and P. Y. Wan, *RSC Adv.*, 2014, **4**, 29917–29924.
32 Y. D. Xue, Y. Zhang, Y. Zhang, S. L. Zheng, Y. Zhang and W. Jin, *Chem. Eng. J.*, 2017, **325**, 544–553.
33 S. O. Ganiyu and M. G. El-Din, *Appl. Catal., B*, 2020, **279**, 119366–119376.
34 G. Dodekatos, S. Schünemann and H. Tüysüz, *ACS Catal.*, 2018, **8**, 6301–6333.
35 L. Wang, S. Y. Liu, H. M. Jiang, Y. Y. Chen, L. A. Wang, G. Y. Duan, Y. Z. Sun, Y. Y. Chen and P. Y. Wan, *J. Electrochem. Soc.*, 2018, **165**, H705–H710.
36 L. Wang, Y. M. Chen, S. Y. Liu, H. M. Jiang, L. A. Wang, Y. Z. Sun and P. Y. Wan, *RSC Adv.*, 2017, **7**, 51419–51425.
37 E. E. Switzer, R. Zeller, Q. Chen, K. Sieradzki, D. A. Buttry and C. Friesen, *J. Phys. Chem. C*, 2013, **117**, 8683–8690.
38 I. M. AlNashef, M. L. Leonard, M. C. Kittle, M. A. Matthews and J. W. Weidner, *Electrochem. Solid-State Lett.*, 2001, **4**, D16–D18.
39 A. S. Barnes, E. I. Rogers, I. Streeter, L. Aldous, C. Hardacre, G. G. Wildgoose and R. G. Compton, *J. Phys. Chem. C*, 2008, **112**, 13709–13715.
40 D. Zhang, T. Okajima, F. Matsumoto and T. Ohsaka, *J. Electrochem. Soc.*, 2004, **151**, D31–D37.
41 Y. Q. Zhang, F. Huo, Y. L. Wang, S. J. Zhang and H. Y. He, *Front. Chem.*, 2019, **7**, 78.
42 M. Kathiresan and D. Velayutham, *Chem. Commun.*, 2015, **51**, 17499–17516.
43 Y. Y. Sun, I. Sinev, W. Ju, A. Bergmann, S. r. Dresp, S. Kühl, C. Spöri, H. Schmies, H. Wang, D. Bernsmeier, B. Paul, R. Schmack, R. Kraehnert, B. R. Cuenya and P. Strasser, *ACS Catal.*, 2018, **8**, 2844–2856.
44 H. M. Jiang, L. Wang, L. L. Qiao, A. G. Xue, Y. J. Cheng, Y. Y. Chen, Y. Ren, Y. M. Chen and P. Y. Wan, *Int. J. Electrochem. Sci.*, 2019, **14**, 2645–2654.
45 X. Z. Yuan, V. Alzate, Z. Xie, D. G. Ivey, E. Dy and W. Qu, *J. Electrochem. Soc.*, 2014, **161**, A458–A466.
46 A. Khan, X. Y. Lu, L. Aldous and C. Zhao, *J. Phys. Chem. C*, 2013, **117**, 18334–18342.
47 A. W. Taylor, P. Licence and A. P. Abbott, *Phys. Chem. Chem. Phys.*, 2011, **13**, 10147–10154.
48 J. Jacquemin, P. Husson, A. A. H. Pádua and V. Majer, *Green Chem.*, 2006, **8**, 172–180.
49 S. Fendt, S. Padmanabhan, H. W. Blanch and J. M. Prausnitz, *J. Chem. Eng. Data*, 2011, **56**, 31–34.
50 A. Ejigu and D. A. Walsh, in *Electrochemistry in Ionic Liquids*, Springer, 2015, pp. 483–506.
51 E. T. Saka, G. Çelik, G. Sarkı and H. Kantekin, *J. Inclusion Phenom. Macrocyclic Chem.*, 2016, **85**, 161–168.
52 S. Steenken and P. Neta, *J. Phys. Chem.*, 1982, **86**, 3661–3667.
53 M. Leopoldini, T. Marino, N. Russo and M. Toscano, *J. Phys. Chem. A*, 2004, **108**, 4916–4922.
54 T. A. Enache and A. M. Oliveira-Brett, *J. Electroanal. Chem.*, 2011, **655**, 9–16.
55 L. J. Ma, Z. H. Wang and Q. M. Li, *Analyst*, 2012, **137**, 432–436.
56 R. Zarrougui, M. Dhahbi and D. Lemordant, *J. Solution Chem.*, 2015, **44**, 686–702.
57 A. M. O'Mahony, D. S. Silvester, L. Aldous, C. Hardacre and R. G. Compton, *J. Chem. Eng. Data*, 2008, **53**, 2884–2891.
58 M. J. Santos, M. C. Medeiros, T. M. Oliveira, C. C. Morais, S. E. Mazzetto, C. A. Martínez-Huitle and S. S. Castro, *Electrochim. Acta*, 2016, **212**, 95–101.
59 P. B. Hao, M. J. Zhang, W. Zhang, Z. Y. Tang, N. Luo, R. Tan and D. H. Yin, *Catal. Sci. Technol.*, 2018, **8**, 4463–4473.
60 M. L. Gao and H. Z. Li, *Green Chem.*, 2007, **9**, 421–423.
61 C. Bock and B. MacDougall, *J. Electrochem. Soc.*, 1999, **146**, 2925–2932.

62 R. Kötz, S. Stucki and B. Carcer, *J. Appl. Electrochem.*, 1991, **21**, 14–20.
63 K. Miki, V. Renganathan and M. H. Gold, *Biochemistry*, 1986, **25**, 4790–4796.
64 D. V. Evtuguin, A. I. Daniel, A. J. Silvestre, F. M. Amado and C. P. Neto, *J. Mol. Catal. A: Chem.*, 2000, **154**, 217–224.
65 D. F. Gao, P. F. Wei, H. F. Li, L. Lin, G. X. Wang and X. H. Bao, *Acta Phys.–Chim. Sin.*, 2021, **37**, 2009021.
66 Z. W. Wu, W. L. Ding, Y. Q. Zhang, Y. L. Wang and H. Y. He, *Acta Phys.–Chim. Sin.*, 2020, **36**, 2002021.
67 Y. Q. Zhang, H. Y. He, K. Dong, M. H. Fan and S. J. Zhang, *RSC Adv.*, 2017, **7**, 12670–12681.
68 M. J. Frisch, G. W. Trucks, H. B. Schlegel, G. E. Scuseria, M. A. Robb, J. R. Cheeseman, G. Scalmani, V. Barone, B. Mennucci, G. A. Petersson, H. Nakatsuji, M. Caricato, X. Li, H. P. Hratchian, A. F. Izmaylov, J. Bloino, G. Zheng, J. L. Sonnenberg, M. Hada, M. Ehara, K. Toyota, R. Fukuda, J. Hasegawa, M. Ishida, T. Nakajima, Y. Honda, O. Kitao, H. Nakai, T. Vreven and J. A. Montgomery, *Gaussian 09, Revision D.01*, Gaussian Inc., Wallingford CT, 2013.